Gigahertz Large-Area-Electronics RF Switch and its Application to Reconfigurable Antennas

Can Wu, Yue Ma, Suresh Venkatesh, Yoni Mehlman, Sigurd Wagner, James C. Sturm, Naveen Verma
Department of Electrical Engineering, Princeton University, Princeton, NJ, 08540, USA

***Abstract*—**Future IoT and 5G networks place significant new demands on antennas, where unguided EM waves are generated to access densely distributed sensor nodes. Reconfigurable antennas, capable of changing key parameters (directionality, frequency response, polarization), are starting to play a critical role, but are limited by the assembly of discrete RF components across the large antenna apertures typically desired. This work presents the design, and use in a reconfigurable antenna, of RF switches for 2.4 GHz-band wireless applications, based on large-area-electronics (LAE) zinc-oxide (ZnO) thin-film transistors (TFTs). ZnO TFTs can be fabricated monolithically on meter-scale and flexible substrates, as done in flat panel displays, but where their frequencies have been limited to 10's of MHz. RF switch performance is enabled for ZnO TFTs (fabricated at flex-compatible temp. <200°C) via self-aligned processing, thick-composite gate electrodes, breakdown-safe biasing, and resonant operation, leveraging high-Q LAE inductors. Reconfigurable antenna radiation patterns are demonstrated.

I. Introduction and RF Switch Application

IoT/5G networks envision wireless sensing from a large number of densely distributed nodes, to control on-demand delivery of high-bandwidth content. Accessing sensors, typically in the 2.4 GHz band, raises critical requirements (such as direction finding/steering, spectrum allocation, etc.), motivating reconfigurable antennas that are capable of changing key parameters (directionality, frequency response, polarization), to meet simultaneous constraints[1].

Such parameters are enhanced by scaling the ratio of the antenna dimension to the signal wavelength (D/λ, with $\lambda =$ 12.5 cm at 2.4 GHz). This motivates the use of LAE, which can enable meter-scale and flexible monolithic implementation, to overcome scalability and reliability limitations of today's approaches based on integrating discrete active devices[2,3]. (LAE displays today are processed on glass ~10 m^2 in size.)

Fig. 1 shows the demonstrated reconfigurable antenna, which employs RF switches based on LAE ZnO TFTs on glass operating at 2.4 GHz. The antenna consists of the ZnO TFT RF switches between electrically-small metal patches in a 2-D array. With the two central patches driven by a differential RF input, changing the ON/OFF states of the switches redistributes the surface current and alters the effective aperture, which together determine the far-field radiation pattern, resonant frequency, bandwidth, and polarization of the radiated signal.

A primary challenge is maintaining large-area fabrication compatibility while boosting the TFT operating frequency, from the 10's of MHz, typical in flat-panel display applications, to the 2.4 GHz range required for practical wireless sensing systems. This is achieved as described in the next section.

II. LAE RF Switch Design

RF switches are implemented in LAE using low-temperature-processed (<200 ºC) bottom-gate ZnO TFTs (similar to the display industry), with a design goal of maximizing the impedance ratio between the OFF and ON states $|Z_{OFF}(\omega)/Z_{ON}(\omega)|$. This is achieved by high-frequency TFT design, exploiting the passive nature of switches within the designed antenna architecture, and by high-Q inductors enabled by LAE.

High-frequency Device Design

Our ZnO TFTs (structure in Fig. 2(a)) consist of a parasitic C_{GD}-R_{PAR}-C_{GS} branch in the OFF state ($V_{GS} < V_T$), while the ON state ($V_{GS} > V_T$) includes an additional R_{CH} branch (Fig. 2(b)), where: C_{GD}/C_{GS} are gate-to-drain/source overlap capacitances; $R_{PAR} = R_G^L + 2R_C$ is a parasitic resistance resulting from gate metal in the longitudinal direction (R_G^L) and source/drain contacts (R_C); R_{CH} is the ON-state channel resistance.

To isolate the impact of each design parameter, for the OFF-state the parasitic branch is transformed at the frequency of interest (i.e., 2.4 GHz) to parallel $C_{PAR,||}$ and $R_{PAR,||}$. Fig. 3 illustrates how the impedance of $C_{PAR,||}$ and $R_{PAR,||}$ vary with R_{PAR} at 2.4 GHz. First, to maximize $R_{PAR,||}$ requires either minimizing or maximizing R_{PAR}, which is set by the longitudinal gate resistance R_G^L (since contact resistance R_C is kept low to reduce the ON-state resistance). Maximizing R_G^L is ruled out because: (1) the resulting large RC time constant of ~milliseconds will cause unacceptably slow switching transitions; and (2) the resulting excessive transverse gate resistance prevents robust V_{GS} biasing along the TFT width ($R_G^T > 100\ M\Omega$ for $R_{PAR} > 22\ \Omega$, shaded region of Fig. 3). Hence, R_{PAR} is minimized via a thick gate stack, composed of Cr/Al/Cr (10/110/40 nm), with Al providing low resistivity and Cr providing proper work function and substrate adhesion. Further, a multi-finger gate is adopted to minimize R_G^T.

With a minimized R_{PAR}, next consider $C_{PAR,||} \approx 1/(1/C_{GD} + 1/C_{GS})$. To maximize $|Z_{OFF}|$ ($\approx |1/j\omega C_{PAR,||}|$), C_{GD} and C_{GS} are made as small as possible by self-aligned processing, which reduces the gate-to-source/drain overlap region. In the fabrication process (Fig. 4), the channel is lithographically defined by the gate electrode via UV exposure from the back of the sample, taking advantage of ZnO's UV transparency. This results in overlaps of ~0.5 μm[5], in contrast to 5-10 μm from conventional lithography allowing for substrate size changes due to thermal cycling. TFT modeling in

Fig. 5 shows self-alignment increases $|Z_{OFF}|$ by an order of magnitude, and boosts the cut-off frequency (where $|Z_{OFF}(\omega)| = |Z_{ON}(\omega)|$) by tenfold, from 91 MHz to 910 MHz.

Breakdown-safe Biasing

The TFT breakdown condition (Fig. 6) shows an inverse relationship between V_{DS} and the breakdown I_{DS}, indicating a fixed power P_{BREAK} as the dominant breakdown condition. This is typical of thermally-induced breakdown and relevant with thermally-insulating substrates like glass or plastic commonly-used in LAE.

A key attribute of the reconfigurable antenna architecture is its use of TFTs as passive switches, enabling deep-triode operation with low V_{DS} (low power) as compared with active amplifiers that require saturation-regime operation with much higher V_{DS} (high power). For the latter, close to the thermal-breakdown limit with $V_{GS} = V_{DS} = 6$, the measured TFT f_T/f_{MAX} are 0.4/2.0 GHz (Fig. 7). In contrast, the passive switch with low V_{DS} enables ON-state V_{GS} safely set at 20V, significantly reducing R_{CH} (limited by ${V_{DS}}^2/P_{BREAK}$), while ensuring adequate margin against TFT breakdown. TFT modeling in Fig. 8 shows that this boosts the cut-off frequency from 0.91 GHz to 8.8 GHz.

High-Q Resonant Switch

To further enhance switch performance, resonant operation is exploited to achieve a high $|Z_{OFF}|$, whereby the conductance of the parasitic capacitance $C_{PAR,||}$ is canceled by a high-Q inductors, possible in LAE due to large loop dimensions, wide traces, and thick metal. This effectively trades $|Z_{OFF}/Z_{ON}|$ bandwidth for gain, appropriate for wireless applications which often operate in a narrow band.

Fig. 9 shows a monolithic loop inductor fabricated, by a 200 μm-wide and 2.5 μm-thick gold trace with a radius of 1 mm on a glass substrate, to give an inductance of ~4.1 nH. In parallel with the TFT of Fig. 8, this yields a resonant frequency of 2.4 GHz in the OFF state. The measurements also show a quality factor of ~28 at 2.4 GHz, about three times higher than that of a monolithic inductor with similar geometry in Si-CMOS technology. TFT modeling in Fig. 10 shows this significantly enhances $|Z_{OFF}/Z_{ON}|$ in the frequency band of interest.

III. Measurement Results

As shown in Fig. 11, the RF switches are fabricated at flex-compatible temperature (<200ºC) on glass using TFTs with $W/L = 3000\ \mu m/1.4\ \mu m$ (transfer curve shown in Fig. 12 with statistics summarized in Table 1). A high-valued ~20 kΩ resistor made of Cr film is put in series with the gate to isolate against the DC gate-biasing traces from creating parasitic RF paths and to protect the TFTs from ESD damage. The measured drain-to-source TFT impedances, at $V_{GS} = 0V$, $6V$, and 20V, are shown in Fig. 13. The measured resonant-switch impedance is shown in Fig. 14. Within the band centered at 2.4 GHz $|Z_{OFF}/Z_{ON}|$ ranges from 22 to 48. This demonstrates for the first time the capability of LAE technology to provide effective switching of RF signals at microwave frequencies for practical wireless systems.

The reconfigurable antenna is demonstrated as shown in Fig. 15(a). The 9 cm × 9 cm antenna aperture consists of an 11 × 11 array of 4.2 mm × 4.2 mm metal patches. Between each two neighboring patches, an RF switch is placed to regulate current paths across the array (208 switches in total). The fabrication is fully compatible with monolithic integration of all antenna components on a single large-area and flexible substrate. However, due to the limited size of the microfabrication equipment used for prototyping (6 cm × 6 cm), the fabricated TFTs were diced and assembled onto a custom printed circuit board (PCB) with the metal patches. The PCB carries an aluminum ground plane, a dielectric spacer, the 2-D array of metal patches, the RF input, and the 208 DC voltages (20/0V) for biasing each switch ON/OFF.

Each planar metal patch is a sub-radiator. In its vicinity, the EM field is governed by both currents flowing directly in from its neighbors, as well as surface currents induced by interaction with other patches via near-field coupling. Hence, the overall antenna characteristics, including electrical impedance, polarization, and beam pattern, are controlled by the ON/OFF states of all switches. Full-wave EM simulations are performed (Fig. 16) to show the current distribution and radiation patterns for three representative switch-state configurations.

Far-field measurements of the prototype antenna (setup in Fig. 15(b)) are shown in Fig. 17. The radiation patterns and frequency responses for four representative switch configurations are shown, demonstrating expected control (with switch states determined for the desired characteristics from a genetic-programming algorithm). Table 2 and 3 summarize this work, and compare it to previously demonstrated high-speed TFTs and reconfigurable antennas that are based on discrete assembly of active devices or area-limited technologies. The present work achieves: (1) gigahertz operation of TFTs while maintaining large-area compatibility; and (2) superior or comparable directionality control (steering range and half-power bandwidth) in a monolithically-integrable technology for reconfigurable antennas.

IV. Conclusions

Large-Area Electronics RF switches at 2.4 GHz were designed, fabricated, and incorporated in a reconfigurable antenna demonstration. Dynamically-tunable radiation patterns were generated and measured. This work demonstrates that LAE electronics can be employed in RF systems for future IoT/5G wireless applications.

Acknowledgment

This work was supported by grants from Semiconductor Research Corporation (SRC), DARPA, and Princeton Program in Plasma Science and Technology (PPST). This work also utilized the Princeton PRISM cleanroom facilities.

References

[1] C. G. Christodoulou, et al., *Proc. IEEE* **100**, 2250–2261 (2012).
[2] L. N. Pringle, et al., *IEEE Trans. Antennas Propag.* **52**, 1434–1445 (2004).
[3] D. Rodrigo, et al., *IEEE Trans. Antennas Propag.* **62**, 3422–3427 (2014).
[4] C. Jung, et al. *IEEE Trans. Antennas Propag.* 54.2 (2006): 455-463.
[5] Y. Mehlman, et al. in *75th Device Research Conference (DRC),* 1-2 (2017).
[6] N. Münzenrieder, et al. *IEEE Trans. Electron Devices* 60.9 (2013): 2815-2820.
[7] C. Carta, et al. In *2013 SBMO/IEEE MTT-S International Microwave & Optoelectronics Conference (IMOC), 1-2* (2013).
[8] Y. Wang , et al. *IEEE Trans. Electron Devices* 65.4 (2018): 1377-1382.
[9] M. Wang, et al. In *2019 IEEE International Electron Devices Meeting (IEDM)*, 8.2.1-8.2.4 (2019).

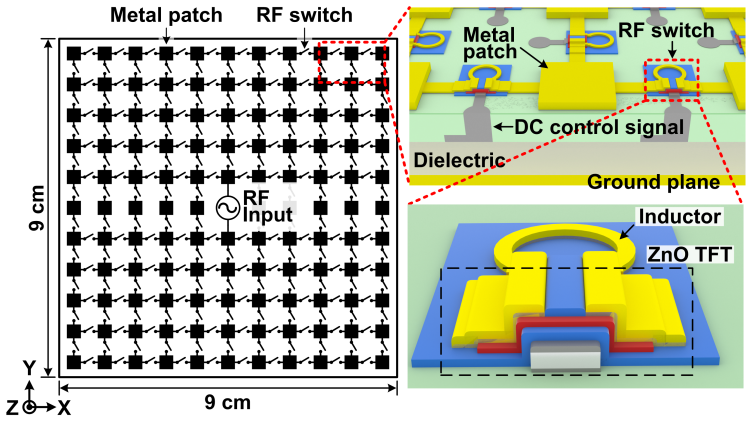

Fig. 1. Left: System schematic of the reconfigurable antenna, consisting of (i) a planar radiating aperture of 11 × 11 metal squares each 4.2 mm on a side, covering 9 cm × 9 cm (0.72λ × 0.72λ at 2.4 GHz); (ii) 208 RF switches connecting neighboring patches; (iii) a single external RF source connected in the middle. Top right: the antenna cross section, with a ground plane to direct radiation towards the upper hemisphere, the metal patches as sub-radiators, and a dielectric layer to improve radiation efficiency. Bottom right: resonant RF switch, consisting of a ZnO TFT and a loop inductor made of Au.

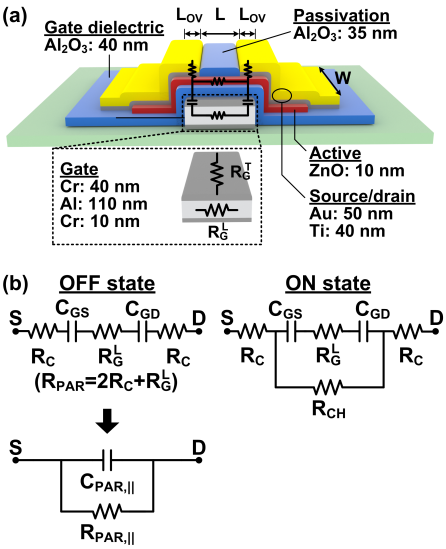

Fig. 2. Impedance analysis of LAE bottom-gate ZnO TFT. (a) Cross-section: the low-resistance gate metal consists of a stack of Cr/Al/Cr. The gate dielectric (Al_2O_3), semiconductor (ZnO), and passivation (Al_2O_3) are deposited by plasma-enhanced atomic layer deposition (PEALD). S/D contacts are Ti/Au. Inset: illustration of longitudinal gate resistance ($R_G^L = R_\square \cdot \frac{L}{W}$, where $R_\square$ is the sheet resistance of the gate metal, and the transverse gate resistance ($R_G^T = R_\square \cdot \frac{W}{L}$). (b) ON/OFF-state circuit model of the ZnO TFT as an RF switch.

Series-to-parallel transformation equations:

① $R_{PAR,||} = R_{PAR} \cdot \left(1 + \frac{1}{\omega^2 C_{DS}^2 R_{PAR}^2}\right)$

② $|Z_{C_{PAR,||}}| = \left|1/\frac{j\omega C_{DS}}{1+\omega^2 C_{DS}^2 R_{PAR}^2}\right|$

③ $C_{DS} = 1/(1/C_{GS} + 1/C_{GD})$

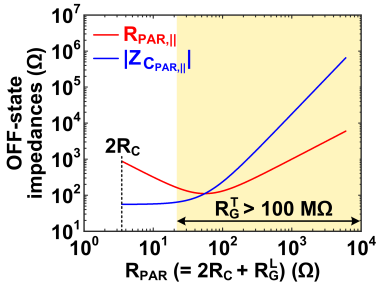

Fig. 3. Analysis of the OFF-state impedance dependence on $R_{PAR}(= 2R_C + R_G^L)$ for TFT with $W/L = 3000\,\mu m/1.4\,\mu m$ at $\omega = 2\pi \cdot 2.4\,GHz$. The yellow region indicates where the values of R_{PAR} cause the transverse gate resistance (R_G^T) to be larger than 100 MΩ, too high for robust gate biasing.

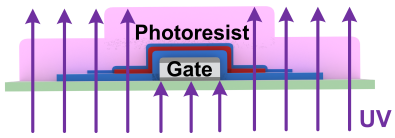

Fig. 4. Schematic of TFT S/D metal patterning, self-aligned to gate via backside exposure screened by the gate metal. Large overlaps are eliminated between S/D and gate. The pink layers are photoresist, while other colors correspond to the layers in Fig. 2(a).

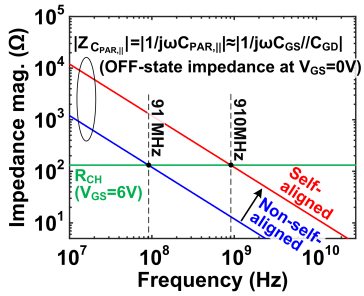

Fig. 5. Modeled impedances of self-aligned and non-self-aligned TFTs with $W/L = 3000\,\mu m/1.4\,\mu m$ (with gate-to-source/drain overlaps of 0.5 µm and 5 µm, respectively), achieving cut-off frequency of 910 MHz by the self-aligned processing.

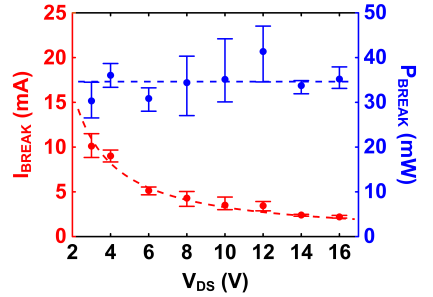

Fig. 6. Measured breakdown I_{DS} (I_{BREAK}) vs. V_{DS} and breakdown power $P_{BREAK} = I_{BREAK} \cdot V_{DS}$ vs. V_{DS}. Constant P_{BREAK} suggests thermal breakdown.

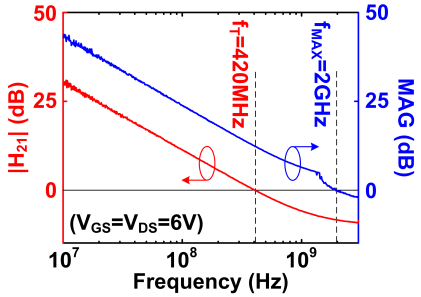

Fig. 7. f_T and f_{MAX} measurement of a typical ZnO TFT with channel width $W = 150\,\mu m$ and channel length $L = 1\,\mu m$ (6 fingers, each 25 µm wide).

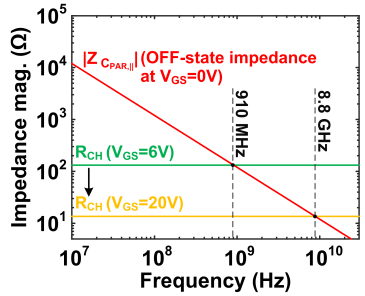

Fig. 8. Modeled impedances of self-aligned TFT with $W/L = 3000\,\mu m/1.4\,\mu m$ at $V_{GS} = 0V$, $6V$, and $20V$, achieving cut-off frequency of 8.8 GHz. Compare trends to measurement results in Fig. 13.

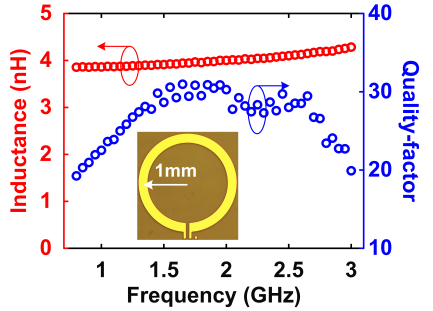

Fig. 9. Measured inductance and quality-factor of the gold loop inductor, with 1 mm radius, 200 µm trace width, and 2.5 µm thickness. Inset: microscope image of the loop inductor.

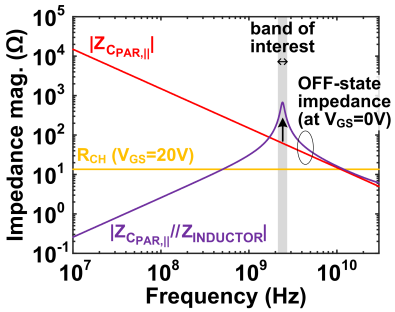

Fig. 10. Modeled impedances of the resonant RF switch. The grey region indicates the frequency band of interest.

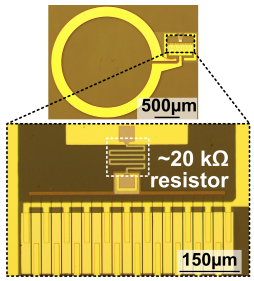

Fig. 11. Microscope image of the LAE-based resonant RF switch, with zoom-in of the TFT and 20 kΩ resistor for gate DC bias (made of a 15 nm-thick Cr trace).

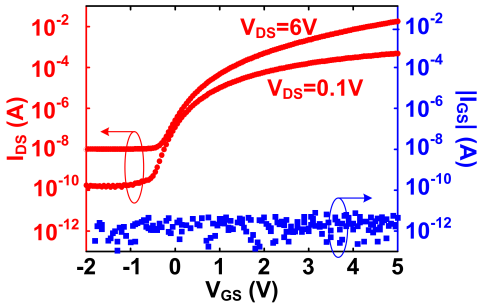

Fig. 12. Measured $I_{DS} - V_{GS}$ transfer curve of ZnO TFT, used in the RF switch, with $W/L = 3000\ \mu m/1.4\ \mu m$.

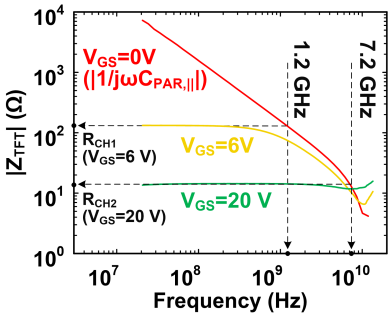

Fig. 13. ZnO TFT impedances at $V_{GS} = 0V$, $6V$, and $20V$, measured by a vector-network analyzer. Compare trends to models in Fig. 8.

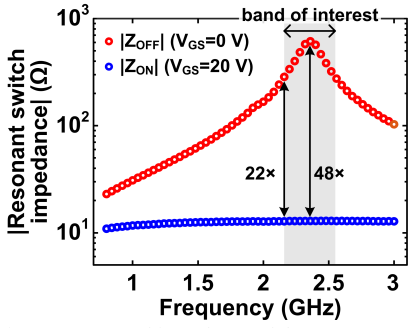

Fig. 14. Measured impedance of the resonant RF switch in the ON and OFF state, at $V_{GS} = 0V$ and $V_{GS} = 20V$, respectively.

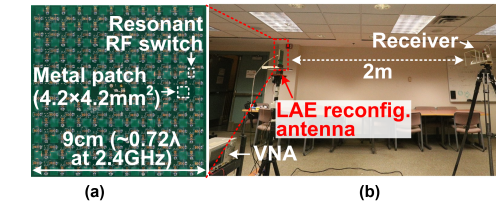

Fig. 15. Images of (a) reconfigurable antenna prototype and (b) setup for measuring far-field (2m distance) radiation pattern. Antenna is placed on motor-controlled turntable and driven at central patch elements by VNA analyzer port. Radiation at each angle is measured by a receiver, employing high-gain horn antenna for reduced sensitivity to multipath, feeding VNA analyzer port.

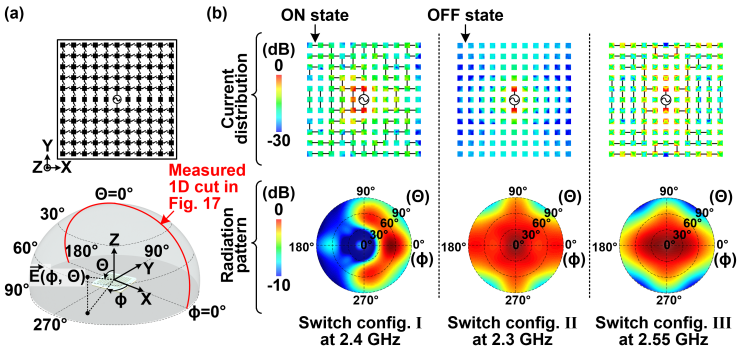

Fig. 16. Full-wave EM simulation of the reconfigurable antenna for three representative switch configurations. (a) Definition of coordinate axes. The antenna sits on the xy plane at z = 0. The radiation pattern is probed on a hemisphere in the far field. (b) Simulated surface current distributions and radiation patterns. The top three plots show the switch configurations (with black lines representing switches that are on), and corresponding current magnitude. The bottom plots show the stereographic projections of the corresponding far-field radiation patterns, with latitude and longitude representing θ and ϕ in (a), respectively.

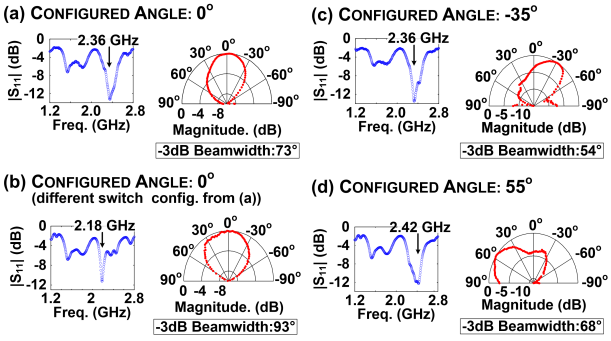

Fig. 17. Measured S_{11}'s (left) and radiation patterns (right) for four representative switch configurations.

W/L (μm/μm)	3000/1.4
Gate-to-S/D overlap (μm)	~0.5
V_T (V)	3.25±0.17
μ_{FE} ($cm^2/V{\cdot}s$)	23.3±5.2
SS (mV/dec)	144.0±15.4
On-off ratio	$>3\times10^6$
Gate leakage	<10 pA

Table 1. Summary of physical dimensions and key figures of merit of 15 ZnO TFTs.

	This work	[6]	[7]	[8]	[9]
Semiconductor	ZnO	IGZO	IGZO	IGZO	ITO
Large-area compatibility	Yes	Yes	Yes	No	No
Channel length	1.4 μm	0.5 μm	1 μm	360 nm	160 nm
Overlap length	0.5 μm	1.55 μm	-	150 nm	300 nm
μ_{FE} ($cm^2/V{\cdot}s$)	23.3	7.5	10	18.2	26
f_T (GHz)	0.4	0.135	0.047	1.2	2.1
f_{MAX} (GHz)	2	-	-	1.1	3.7
Cut-off frequency of RF switch (GHz) (non-resonant)	7.2	-	-	-	-

Table 2. TFT summary, including previous work on high-speed TFTs.

	This work	[2]	[3]	[4]
Technology	LAE	Discrete Si BJT	Discrete Si diode	RF MEMS
Capable of full-aperture monolithic integration over large dimension	Yes	No	No	No
Capable of flexible form factor	Yes	No	No	No
Size of aperture (wavelength)	0.72λ × 0.72λ	0.8λ × 0.8λ	0.72λ × 0.72λ	0.5λ × 0.5λ
Size of aperture (cm)	9 × 9	22.5 × 22	8.7 × 8.7	2.5 × 2.5
Frequency (GHz)	2.1-2.5	0.8-1.5	2.4-3.0	5.7-8.2
Antenna efficiency	33%	63%*	-	-
Static power of switch-control	<5 μW	~10 mW	0.42 W	-
Demonstrated steering range (°)	90	90	60	28
Demonstrated average HPBW (°)	72	76	50	94

Table 3. Antenna summary, including previous work on reconfigurable antennas made with discrete components or area-limited technologies (*the antenna efficiency does not include the significant static power of switch-control).